

Radar Observations of Asteroid 1620 Geographos

STEVEN J. OSTRO, RAYMOND F. JURGENS, AND KEITH D. ROSEMA

Jet Propulsion Laboratory, Pasadena, California 91109-8099

E-mail: ostro@echo.jpl.nasa.gov

*California
Institute of
Technology*

R. SCOTT HUDSON

School of Electrical Engineering and Computer Science, Washington State University,

Pullman, Washington 99164-2752

AND

JONATHAN D. GIORGINI, RON WINKLER, DONALD K. YEOMANS,

DENNIS CHOATE, RANDY ROSE, MARTIN A. SLADE, S. DENISE HOWARD,

DANIEL J. SCHEERES, AND DAVID L. MITCHELL

Jet Propulsion Laboratory, Pasadena, California 91109-8099

July 1995

California Institute of Technology

To be submitted to *Icarus*

<u>Author</u>	<u>AC</u>	<u>voice</u>	<u>fax</u>	<u>JPL mailstop</u>	<u>E-mail</u>
Ostro	818	354-3173	354-9476	300-233	ostro@echo.jpl.nasa.gov
Jurgens	818	354-4974	354-6825	238-420	jurgens@bvd.jpl.nasa.gov
Rosema	818	393-2629	354-9476	300-233	rosema@think.jpl.nasa.gov
Hudson	509	335-0922	335-3818		HUDSON@ECCS.WSU.EDU
Giorgini	818	354-6932	393-1159	301-150	jdgi@tycho.jpl.nasa.gov
Winkler	619	255-8259	255-8515	DSCC-61	winkler@stealth.gdscc.nasa.gov
Yeomans	818	354-2127	393-1159	301-150	Donald.K.Yeomans@jpl.nasa.gov
Choate	619	255-8259	255-8515	DSCC-74	Dennis.Choate@jpl.nasa.gov
Rose	619	255-8259	255-8515	DSCC-61	rose@stealth.gdscc.nasa.gov
Slade	818	354-2765	354-6825	238-420	Martin.A.Slade-III@jpl.nasa.gov
Howard	818	354-3284	354-6825	238-420	howard@radarsun.jpl.nasa.gov
Scheeres	818	354-7128	393-6388	301-1251	djs@leelanau.jpl.nasa.gov
Mitchell	818	354-9474	354-9476	300-233	mitchell@think.jpl.nasa.gov

37 manuscript pages (or 27 excluding tables and figure captions)

11 figures

6 tables

Keywords: asteroids, radar

Running head: RADAR OBSERVATIONS OF GEOGRAPHOS

Send editorial correspondence and proofs to:

Dr. Steven J. Ostro
300-233
Jet Propulsion Laboratory
Pasadena, CA 911 09-8099

voice: (818) 354-3173

fax: (818) 354-9476

E-mail: ostro@echo.jpl.nasa.gov

ABSTRACT

Goldstone radar observations of Geographos from Aug. 28 through Sep. 2, 1994, yield over 400 delay-Doppler images whose linear spatial resolutions range from ~ 75 m to ~ 151 m, and 138 pairs of dual-polarization (OC, SC) spectra with one-dimensional resolution of 103 m. Each data type provides thorough rotational coverage. The images contain an intrinsic north/south ambiguity, but the equatorial view allows accurate determination of the shape of the radar-facing part of the asteroid's pole-on silhouette at any rotation phase. Sums of co-registered images that cover nearly a full rotation have defined the extremely elongated shape of that silhouette (os1 ro *et al.* 199S, *Nature* 375, 474-477). Here we present individual images and co-registered sums over $\sim 30^\circ$ of rotation phase that show the silhouette's structural characteristics in finer detail and also reveal numerous contrast features "inside" the silhouette. Those features include several candidate craters as well as indications of other sorts of large-scale topographic relief, including a prominent central indentation. Protuberances at the asteroid's ends may be related to the pattern of ejecta removal and deposition caused by the asteroid's gravity field. The asteroid's surface is homogeneous and displays only modest roughness at centimeter-to-meter scales. Our estimates of radar cross section and the currently available constraints on the asteroid's dimensions are consistent with a near-surface bulk density between 2 and 3 g cm^3 . The delay-Doppler trajectory of Geographos' center of mass has been determined to about 200 m on Aug. 28 and to about 100 m on Aug. 31, an improvement of two orders of magnitude over pre-observation ephemerides.

1. INTRODUCTION

Asteroid 1620 Geographos was discovered in 1951 by A. G. Wilson and R. Minkowski and was observed over an eight-month interval in 1969 by Dunlap (1974) for “light variation, colors, and polarization. ” From his analysis, which included experiments with laboratory models (Dunlap 1972), he estimated the asteroid’s spin vector and geometric albedo, and noted that “the best fitting model (a cylinder with hemispherical ends) had a length to width ratio of 2.7, which results in Geographos being 1.50 ± 0.15 km wide and 4.0 ± 0.5 km long.” Veeder *et al.* (1989) estimated an effective diameter of 2.7 km on the basis of their 10- μ m radiometry. The asteroid’s original S classification (Chapman *et al.* 1975) from broadband color indices has been refined by CCD spectra (Hicks *et al.* 1995) that indicate either type SII or type S111 in the system of Gaffey *et al.* (1993). Radar observations of Geographos at Arecibo in February and March 1983 (Ostro *et al.* 1991a), shortly before an approach to within 0.09 AU, yielded 13-cm-wavelength estimates of radar cross section and circular polarization ratio as well as delay-Doppler astrometry. Variations in the echo bandwidth were readily apparent, but limited echo strength precluded independent estimation of the asteroid’s dimensions from the echo spectra,

Geographos’ Aug. 25, 1994, approach to 0.0333 AU, the closest for at least the next two centuries, provided a unique opportunity for observations with the Goldstone 3.52-cm (85 10-MHZ) radar. The asteroid entered Goldstone’s declination window on Aug. 28 (Table I) and we observed it daily for a week, concentrating on delay-Doppler imaging on each of the first five dates and continuous-wave (cw), dual-polarization observations on the last two. The predicted signal-to-noise ratios (SNRs) in Table 1 turned out to be fairly accurate and most of our observations yielded useful echoes. The maximum single-date SNR

for Geographos, ~ 1000 , was roughly half that achieved in the Arecibo imaging of 4769 Castalia (Ostro *et al.* 1990a), but much finer resolution was obtained for Geographos in 1994 than for Castalia in 1989. As discussed by Ostro *et al.* (1995), our observations confirm lightcurve-based inferences about Geographos' extreme elongation. Here we describe our experiment in detail and present radar "movies" that reveal a variety of the asteroid's structural characteristics and also yield a refined orbit.

Scheduled many years in advance, this radar experiment was given special impetus by the Clementine mission, which planned a 10.7 km s^{-1} flyby of Geographos on Aug. 31 at a miss distance of approximately 100 km (Nozette and Garrett 1994). We intended to use radar astrometry to improve the pre-encounter ephemeris and to use imaging with complete rotational coverage to optimize the post-encounter physical model of the asteroid. Although a computer malfunction led to cancellation of the flyby, the Goldstone experiment provided practice for supporting future spacecraft reconnaissance of near-Earth asteroids.

Clementine also motivated a 1993-1994 campaign of optical photometry (Magnusson *et al.* 1995). That effort's improved estimate of the asteroid's spin vector was invaluable in planning and executing the Goldstone radar observations. The analysis described here uses preliminary estimates of the sidereal spin period ($P_{\text{sid}} = 0.21763866 \text{ days} = 5.22332784 \text{ h}$) and the pole direction (ecliptic longitude, latitude $\approx 55^\circ, -45^\circ$) that were kindly communicated to us by Magnusson and that, for our purposes, are indistinguishable from the results reported by Magnusson *et al.* (1995; see also Kwiatkowski 1995). Goldstone was within 10° of the asteroid's equatorial plane throughout the radar observations.

2. OBSERVATIONS AND DATA REDUCTION

In all our observations, Goldstone's 70-m antenna (DSS-14) transmitted an approximately 450-kilowatt signal toward the asteroid for a duration several seconds less than the echo's roundtrip time delay (RTT). Then we changed to a receiving configuration and recorded echoes for a comparable duration. The antenna's most sensitive receiving system uses separate transmit and receive horns mounted in the radar cone near the dish's primary focus. To switch from transmit to receive, the subreflector must be rotated, a process that can take up to 20 seconds. Our Aug. 28-30 observations used this system to exploit its sensitive front-end amplifier, a hydrogen maser. On Aug. 31 and Sep. 1, mechanical difficulties with the subreflector forced us to use a single-horn system that has a less sensitive high-electron-mobility-transistor (hemt) front end.

Part of our experiment used continuous-wave (cw) transmissions and produced echo spectra, which can be thought of as one-dimensional images, or brightness scans across the target through a slit parallel to the asteroid's apparent spin vector. The bandwidth of a target's instantaneous echo power spectrum is proportional to the breadth, measured normal to the line of sight, of the target's pole-on silhouette, and measurements of echo edge frequencies as functions of rotation phase can be used to estimate the shape of the silhouette's convex envelope (or hull) as well as the frequency of hypothetical echoes from the asteroid's center of mass (Ostro *et al.* 1988).

Most of our observations used a time-modulated waveform to obtain resolution in time-delay as well as Doppler frequency. The result is a two-dimensional, delay-Doppler image that cuts the target with two orthogonal sets of parallel planes. Any such method divides the three-dimensional target into resolution cells in a manner analogous to the way

one cuts a potato to make french fries. Optical imaging is a one-to-one mapping from surface to image, that is, for each image pixel one knows *a priori* that there is a single corresponding surface region. For delay-Doppler imaging, on the other hand, the cells are orthogonal to the line of sight and parallel to the plane of the sky, aligned with the projection of the apparent spin vector. Thus, it may be possible for the radar to see both ends of the cell. For very irregular objects the radar may even see surface elements that lie inside the cell between these ends, e.g., if the cell slices through the sides of a crater. The result is that a delay-Doppler image is generally a many-to-one mapping that contains a form of global aliasing referred to as the north/south ambiguity, and one cannot know, *a priori*, how many points on the surface contributed echo power to a given pixel. Therefore, modeling is usually required to resolve the ambiguity and to allow accurate interpretation of images (Hudson, 1993; Hudson and Ostro 1994). However, in the special case of the equatorial geometry we had for Geographos, the delay-Doppler cells maintain the same orientation with respect to the surface as the object rotates. Therefore, different images can be registered and summed without introducing any distortion beyond the north/south ambiguity described above.

Radar System, Setups, and Signal Processing

Each delay-Doppler observation used a repetitive, binary-phase-coded cw waveform (e.g., Ostro 1993 and references therein) with a 127-element code and one of four time resolutions, or “bauds” ($\Delta t = 7.125, 7.0, 1.0, \text{ or } 0.5 \mu\text{s}$; $1 \mu\text{s}$ provides 150 m of range resolution). The most important steps in real-time processing of digitized samples of the received signal’s voltage were decoding via cross-correlation with the transmitted code and spectral analysis with a 64-point FFT. This procedure produced 64×127 arrays of echo power.

Each array's unaliased frequency window equals $1/(RP \times NCOH)$, where the code repetition period, $RP = 127 \Delta t$, defines the waveform's time-delay window and NCOH is the number of RP -long time series of voltage samples that were coherently summed prior to Fourier analysis. Our cw observations used a frequency-switching technique identical to that described most recently by Ostro *et al.* (1992). Table II lists the key characteristics of our set ups. That table uses a conversion factor

$$\text{Hz/km} = (2 |W_{\text{app}}| \cos \delta) / \lambda \quad (1)$$

that was within 0.2% of 19.0 Hz/km throughout the experiment, Here W_{app} is the asteroid's apparent spin vector and δ is the instantaneous, asteroid-centered declination of the radar.

Figure 1 shows a block diagram of the Goldstone radar system, with emphasis on “back-end” processing and data-acquisition. The reduced data have been grouped into files (Table III) that contain single-run sums that have had the noise baseline removed, are normalized to thermal receiver noise, and are tagged with information about the setup and data processing.

Day-By-Day Overview

Geographos was receding from Earth throughout the experiment. Echo strength varies inversely as the fourth power of the target's distance, so our strategy was to begin imaging as soon as possible on the first date, Aug. 28. In any asteroid radar imaging experiment, the optimal setup (that is, the proper choice of window and resolution in time and frequency) depends on the target's delay-Doppler dispersion, the echo strength, and the accuracy of the

delay-Doppler prediction ephemerides. Normally, one uses a conservative, coarse-resolution setup to attempt initial detection of an asteroid, assesses the coarsely resolved echo signature and the caliber of the delay-Doppler ephemeris, and then proceeds to higher-resolution setups. Practical considerations throughout this process are data-acquisition capabilities, including recording rate and the turnaround time for data inspection.

The Goldstone transmit window on Aug. 28 was only 2.7 h, allowing little time to try different setups. Fortunately, excellent prior knowledge of the target's size and rotation led us to expect the echo's delay-Doppler dispersions to vary between (27 Hz x 14 μ s) and (77 Hz x 5 ps). Also, the formal uncertainties in the delay-Doppler prediction ephemerides, which had been calculated from an orbit based on all optical and radar astrometry through Aug. 17, were only 70 μ s and 1 Hz, and the Goldstone radar data acquisition system was equipped with a flexible real-time display. Our initial, "coarse-baud" (7- and 7.125- μ s) setups were designed to place only a few cells on the asteroid, to ensure that the echo would be easy to see in one or two transmit-receive cycles (runs). Strong echoes were seen immediately.

The long-baud setups had frequency windows an order of magnitude larger than the expected echo bandwidth and three orders of magnitude larger than the expected Doppler uncertainty in the ephemerides. With any repetitive "ranging" waveform, the time-delay correction to the ephemeris is determined modulo the RP. The RP of each of our long-baud setups was about 0.9 μ s, an order of magnitude larger than the formal delay-prediction uncertainty, and the *joint* delay-correction ambiguity from the 7- and 7.125- μ s runs (the product of their respective RPs) was 0.8 s. Therefore, several runs with each of these two setups permitted estimation of an unambiguous delay correction: approximately -84 μ s for the leading edge of the echo. That is, the asteroid was about 13 km closer than predicted. These

statements ignore the waveform's impulse response and gloss over the fact that the delay corresponding to hypothetical echoes from asteroid's center of mass (COM) exceeds the echo's leading-edge delay by some amount that depends on target shape and orientation. Yet, this first measurement disclosed that the accuracy of the delay ephemeris was comparable to its formal uncertainty, a result that would have raised confidence in navigation of Clementine toward Geographos.

The long baud's -17-Hz frequency cells slightly resolved the echo, which appeared centered very close to the ephemeris prediction, an unsurprising result given the Doppler-prediction uncertainty of ~ 1 Hz. The Doppler frequency $\nu(t)$ is related to the time delay $\tau(t)$ by

$$d\tau(t) / dt = -\nu(t) / F_{TX} \quad (2)$$

where Goldstone's transmitter frequency $F_{TX} = 8510$ MHz. Therefore, a Doppler correction of $\Delta\nu_{\text{eph}} = 1$ Hz corresponds to a delay correction rate of $d\Delta\tau_{\text{eph}}(t) / dt = -0.423 \mu\text{s/h}$. The rate of motion of a target's COM with respect to the delay-prediction ephemeris determines the smearing of an image built up from a given signal integration time. The formal Doppler-prediction uncertainty corresponded to less than $0.01 \mu\text{s}$ of smear in the longest RTT in our experiment, so we expected that single-run images would not be smeared noticeably by "ephemeris drift." That the actual Doppler correction was less than 4 Hz became evident as soon as we had imaged the asteroid on different dates at similar rotation phases.

The balance of Aug. 28, all of Aug. 29, and the first 15 minutes on Aug. 30 were devoted to imaging with the $1 \mu\text{s} \times 2.86\text{-Hz}$ setup, which nominally provided $150\text{-m} \times 151\text{-m}$ cells. These observations' 151 useful runs provided thorough rotational coverage.

Geographos' elongation and rotation were immediately apparent from the real-time displays. Predictions of epochs of end-on and broad-side phases that had been communicated to us by P. Magnusson were seen to be accurate.

On Aug. 30 and 31 we used the $0.5\mu\text{s} \times 1.64\text{-Hz}$ setup, which nominally provided $75\text{-m} \times 86\text{-m}$ cells. In our single-run images, rotational smearing of the asteroid's tips is typically about 25 m and no more than $0.9 \Delta t$ meters, where Δt (seconds) is the run's integration time (Table 111). These higher-resolution images reveal more structural detail than the $1\text{-}\mu\text{s}$ images, but are also noisier. After the Aug. 30 observations, all available optical astrometry, the 1983 radar astrometry, and our "eyeballed" time-delay estimates from the first three days' $1\text{-}\mu\text{s}$ results were input into JPL's On-Site Orbit Determination program (OSOD) to generate refined delay-Doppler prediction ephemerides, which were used for the balance of our observations. We designate the orbit solution used for the Aug. 28-30 observations as OS01-18, that for Aug. 31- Sep. 3 as OS011-22, and the corresponding delay-Doppler ephemerides as E-18 and E-22.

The circular polarization ratio, μ_c , of echo power received in the same sense of circular polarization as transmitted (the SC sense) to the opposite (OC) sense, is a measure of the target's near-surface, wavelength-scale roughness. This ratio was known to be about 0.2 at 13 cm (Ostro *et al.* 1991a); during the first four Goldstone days, high SNR was a priority and we received only OC echoes. On Sep. 1 we tried SC imaging with the $1\text{-}\mu\text{s}$ setup and then, because those echoes were so weak, with the $7\text{-}\mu\text{s}$ setup. On Sep. 2 we changed to a cw configuration that used parallel receiving systems to record SC and OC power spectra simultaneously. Those spectra yielded our most reliable estimates of μ_c and the OC radar cross section σ_{oc} .

Phase Convention

In the following discussion, rotation phase O is referenced to the asteroid's orientation at an epoch, 1994 Aug. 30.032, that had been predicted by Magnusson (pers. comm., Aug. 1994) to correspond to the end-on orientation of a lightcurve-based model ellipsoid near primary (dimpest) lightcurve minimum mI , which follows primary (brightest) lightcurve maximum MI . Magnusson *et al.* (1995) note that Geographos lightcurves consistently show extrema in the chronological order $ml, M2, m2, MI$, corresponding to phases near $0^\circ, 90^\circ, 180^\circ$, and 270° . Table III gives the phase interval spanned by runs in each data file.

3. RESULTS

CW Spectra: Radar Cross Section and Polarization Ratio

The 138 useful runs on Sep. 2 yielded OC/SC spectra that span 1.25 rotations and sample phase thoroughly except for a 25° gap just before the “ mI orientation” ($\sim O^0$). Figure 2 shows the spectra smoothed to 6-Hz resolution. There is a prominent, more than twofold variation in echo bandwidth. Weighted sums of these spectra, plotted in Fig. 3 at the raw frequency resolution (1.95 Hz), yield estimates of the asteroid's average 3.5-cm disc-integrated properties, $\mu_c = 0.22 \pm 0.01$ and $\sigma_{oc} = 0.71 \pm 0.21 \text{ km}^2$, whose uncertainties overlap those of the 13-cm estimates, $\mu_c = 0.19 \pm 0.05$ and $\sigma_{oc} = 0.930.3 \text{ km}^2$. Thus the radar sees similar surface properties at the two wavelengths.

Figure 4 plots single-run estimates of OC, SC, and total-power radar cross sections vs. rotation phase. The variations in $\sigma_{oc}(\theta)$ are pronounced and synchronized with the bandwidth variations. Some of the noiselike fluctuation in the OC radar “lightcurve” may be due to small

(-15'') variations in pointing accuracy. The sampling of θ is finest in an interval, 155° to 230° , that was covered twice, but the fluctuations in $\sigma_{oc}(\theta)$ there appear to be only slightly more severe than elsewhere, lending confidence to the antenna's pointing stability and our data's calibration.

Figure 5 plots the ± 1 standard-deviation envelope on single-run estimates of the SC/OC ratio vs. phase, as well as a five-run running average of the ratio estimates themselves. Run-to-run variations of a few tens of percent in μ_c are common and are somewhat more severe in the phase region covered twice. The scatter is large within each of the independent sequences that covered this region, but there is no systematic difference between the sequences. The fluctuations in $\mu_c(\theta)$ probably arise primarily from the intrinsic noise in the single-run estimates. In summary, the asteroid's near-surface roughness appears uniformly moderate at centimeter-to-meter scales.

Hull Estimation

We have used our cw spectra to estimate the convex envelope, or hull, on Geographos' pole-on silhouette (Ostro *et al.* 1988, 1990b). The central idea of this technique is that the difference, $p_+ = f_+ - f_{COM}$, between the frequencies corresponding to echoes from the approaching limb and the COM, is proportional to the distance of the approaching limb from the plane that contains the apparent spin vector and the radar line of sight. The support function $p(\theta) = p_+(\theta) = p_-(\theta + 180^\circ)$ is periodic and satisfies $p(\theta) + p''(\theta) = r(\theta)$, where $r(\theta)$ is the radius of curvature of the hull at its approaching limb and the primes denote, differentiation with respect to θ . Cartesian coordinates of the hull are given by $x = p \cos \theta - p' \sin \theta$, $y = p \sin \theta + p' \cos \theta$. The hull is convex, so $r(\theta) \geq 0$.

To estimate the hull, we first measured the innermost zero-crossings of each OC spectrum; these numbers define a data vector \mathbf{p}_{dat} for any given choice of f_{COM} . We used weighted least squares to fit a 10-harmonic Fourier model, \mathbf{p}_{unc} , to \mathbf{p}_{dat} . Then we found another Fourier model, \mathbf{p}_{con} , that was constrained to correspond to a non-negative radius-of-curvature function and was as close as possible to \mathbf{p}_{unc} . This entire process was repeated for enough trial values of f_{COM} to define the minimum value of the weighted sum of squares of the residuals, $\chi^2 = (\mathbf{p}_{\text{con}} - \mathbf{p}_{\text{dat}})^T (\mathbf{p}_{\text{con}} - \mathbf{p}_{\text{dat}}) / \mathbf{s}^T \mathbf{s}$, where T denotes transpose and the edge-frequency measurement noises was assumed to be proportional to the noise in the parent spectrum.

Figure 6 shows our hull estimate and associated quantities. Excellent prior knowledge of Geographos' spin vector provides a conversion factor, 18.95 Hz/km, that establishes the scale of the hull estimate, so kilometers are natural units for that figure. The constrained Fourier coefficients are nearly indistinguishable from the unconstrained ones, an outcome of the strength and phase coverage of the spectra. The hull's extreme breadths, within 10% of 5.1 and 2.0 km, or 96 and 38 Hz, occur at phases (mod 180°) of 90° and 178°. Weighted sums of spectra in several-degree intervals centered close to those phases are shown in Fig. 7.

The estimated offset of the COM frequency from the prediction of our E-22 ephemeris is -0.01 ± 0.50 Hz, equivalent to 0 ± 26 m; the assigned uncertainty is based on the shape of $\chi^2(f_{\text{COM}})$ near its minimum and is intended to be conservative. This Doppler correction was useful in analysis of the delay-Doppler images.

Single-Run Images

Data values for each image in this paper are mapped onto a 256-level gray scale. Since the noise background is not interesting, all data values below a clipping level near the noise mean are mapped to black to make the most of the grayscale's available dynamic range. Similarly, all data values above some saturation level are mapped to white, since contrast at the very highest echo levels contains less interesting information than contrast among the more abundant, dimmer pixels. A histogram at the bottom of each image indicates the original distribution of data values, and a gray scale immediately above the histogram indicates the color mapping for each of the histogram bins. Additional labels beneath the histogram provide the actual data value at which clipping occurs and the level at which data values saturate to white, both as a percentage of the brightest data value and as an actual data value.

Figure 8 shows a collage of most of our 1- μ s images from individual runs (Table III). The nearly equatorial view and prior knowledge of the spin period simplifies geometry of the delay-Doppler projection. The distribution of brightness that the radar sees is collapsed onto the asteroid's equatorial plane, forming the images presented here. We view the images from a vantage point out of that plane, looking along the spin vector at a superposition of echoes from the asteroid's northern and southern "hemispheres." Time delay (range) increases from top to bottom, and Doppler frequency (radial velocity) increases from right to left, so the asteroid rotates clockwise. Parts of the asteroid facing away from the radar are unilluminated and hence invisible. Runs within any given data file were typically separated by about two minutes, or about 2.3° of rotation phase.

The asteroid's rotation is evident over the course of the radar movie, but changes in the delay-Doppler signature as a function of phase happen most rapidly near the end-on orientations. The echoes' leading edges are extremely bright at the broadside phases ($M1$, $M2$) but inconspicuous at the end-on phases ($m1$, $m2$). To some degree, this is probably due to the fact that, at ~ 100 -m scales, surface curvature in the equatorial plane is more severe at the ends of this very elongated object. If the orthogonal component of curvature is also severe there, we would certainly expect the leading edges to be much weaker at end-on phases than at broadside phases. Local differences in near-surface bulk density or in the distribution of slopes at scales well below 100 m may or may not share some responsibility for the weak end-on echoes.

Apart from the asteroid's gross dimensions, one of its most interesting characteristics is the disparity between the shapes of its two long sides. The $M2$ side appears nearly convex with only modest variations in curvature, but the middle of the $M1$ side contains a prominent indentation close to a sharp bend, giving the side the appearance of a piece-wise-linear S. In Fig. 2, the spectral peak predominantly left of center from 210° to 235° is due to strong echoes from the receding side's elbow,

Summation of single-run images is desirable to reduce the background noise, especially near the end-on phases. Formation of multi-run sums is mandatory throughout our Aug. 31 and Sep. 1 sequences of $0.5\text{-}\mu\text{s}$ images (Fig. 10), whose noisiness is due to the finer delay-Doppler resolution and to the asteroid's greater distance on those days. Precise knowledge of the rotation period makes rotational co-registration of images straightforward. Of greater concern is translational smearing caused by imperfect knowledge of the delay-Doppler location of the COM in each image. Our delay-Doppler prediction ephemerides

were accurate enough to prevent perceptible, translational smearing over time scales of order 0.2 h, even for the 0.5- μ s setup. To form longer summations, e.g., to construct an estimate of the pole-on silhouette (Ostro *et al.* 1995) or to superpose images from different days, we require an a *posteriori* ephemeris that is at least two orders of magnitude more accurate than our a *priori* ephemerides.

Image Co-Registration: COM Astrometry and Orbit Refinement

As noted earlier, the Aug. 28-30 echoes were drifting through our E-18 ephemeris. Comparison of E-18 with the more accurate E-22 suggested that the rate of change of the COM delay correction was of order $0.7 \mu\text{s h}^{-1}$ (equivalent to -1.7 Hz) on Aug. 28 and about 20% slower on Aug. 29. In forming multi-run sums, error in the COM position in any frame introduces smear. Therefore we experimented with various approaches to estimating each frame's COM position in the Aug. 28 and 29 images, with the intention of feeding the resultant COM astrometry into OSOD, generating an ephemeris much more accurate than E-22, and using COMS predicted by the refined ephemeris to co-register multi-run sums. One strategy was to estimate the pole-on silhouette's hull from the images' leading-edge delays and/or spectral edge frequencies. That approach proved unwieldy compared to the CW hull estimation, in part because of the coarser spatial resolution and less complete phase coverage of the images. A more fruitful approach was to estimate the shape of the pole-on silhouette itself, which we modeled in terms of a 20-harmonic Fourier approximation to the distance from the COM to the silhouette along the radar line of sight at rotational phase ϕ . In this least-squares estimation, our data were the delay-Doppler positions of leading-edge thresholds in the echo-containing frequency bins of each 1- μ s image. For each day, we enforced the

coupling (Eqn. 2) between the Doppler correction and the rate of change of the delay correction, thereby reducing the number of free parameters to four: the delay correction at the mid-receive epoch of each day's first imaging run and the Doppler correction for each day.

The advantage of silhouette estimation over hull estimation is that it uses more information and thus provides more leverage in determining the COM's trajectory through our E-18 ephemeris. However, silhouette estimation does not use echo-containing image pixels at delays past the leading edge. (The total number of echo-containing pixels is typically several times the number of leading-edge pixels.) This shortcoming is overcome by Hudson's (1993) reconstruction technique, previously applied to Castalia (Hudson and Ostro 1994), for simultaneously estimating the asteroid's three-dimensional shape, rotation, radar scattering law, and COM trajectory through the ephemeris. Ideally, that inversion would use all the available radar images, as well as optical lightcurves, but those calculations are very CPU-intensive and have not yet been done. Here we make use of a preliminary estimation designed to constrain the COM trajectory in our 1- μ s images. This 3-D estimation used sums of single-run images within 10° phase intervals.

The differences between the two approaches' delay-Doppler corrections are comparable to or smaller than the imaging resolution (Table IV). The results indicate that the Doppler correction to E-18 was less severe on Aug. 29 than on Aug. 28. The Doppler correction to E-22 from the cw hull estimation, in combination with comparison of the E-22 and E-18 ephemerides, indicated that this trend continued throughout the week. That is, the delay correction was changing nonlinearly, so the Doppler correction was also changing,

Armed with COM astrometry from Aug. 28, Aug. 29, and Sep. 2, we used OSOD to recalculate the orbit. For the August dates, we averaged the corrections from the 2-D and 3-D

modeling and adopted their difference as uncertainties. Table V lists the 1994 radar astrometry that was combined with 1983 radar astrometry and all optical astrometry reported through Aug. 28, 1994, in a new OSOD solution (Table VI) that we will refer to as E-34. The postfit residuals for our astrometry are all less than our assigned uncertainties (Table V). Numerical experiments with the 2-D and 3-D models and with OSOD suggest that errors in the E-34 predictions of the COM's delay-Doppler trajectory do not exceed $2\ \mu\text{s}$ (300 m) or 1 Hz ($17\ \text{mm s}^{-1}$) on Aug. 28 and become smaller on subsequent days. The worst smearing of any of the images discussed here is comparable to or less than the imaging resolution itself.

Multi-run Sums of Images

Figure 9 shows 12 sums of images within $30''$ phase blocks centered on integral multiples of 30° . Here, in addition to the gross characteristics of the *M1* and *M2* sides, we can see knoblike protrusions at the ends of the silhouette, small concavities on the M2 side, and interesting structure along the radar terminator.

Figure 11 shows multi-run sums of our $0.5\text{-}\mu\text{s}$ images, again within 30° phase groups. The three panels contain images from (a) Aug. 30, (b) Aug. 31, and (c) both days. The two-day panel provides higher SNR and fuller phase coverage (Table 11 I), but may contain some blurring from misregistration of images from the two days.

4. DISCUSSION

Contrast Features

In the delay-Doppler projection, concavities tend to be most prominent at higher angles of incidence and even very shallow relief might be perceptible toward the target's limb, We have spent much time examining versions of our images processed with assorted clipping levels, stretches, and smoothing windows. Our subjective impression is that most of the contrast is due to topographic relief. For example, the break in the brightness of the M2 side's leading edge is prominent at both of our imaging resolutions (frame 6 of Figs. 9 and 11 a,c). The *silhouette's* departure from convexity at that location is about 300 m long and less than 100 m deep; the extension of the dark band well inside the silhouette suggests prominent negative relief in the three-dimensional figure.

Some shape characteristics are suggested by the frame-to-frame evolution of image features. For example, the region directly to the right of the COM, toward the *MI* indentation, is unilluminated at both end-on phases, but an island of echo is evident below it at 0° and a different island of echo is evident above it at 180° . The region is partially illuminated at 210° , strongly illuminated from 240° to 300° , and poorly illuminated at 330° . This pattern suggests that the region directly to the right of the COM is a depression of some sort. Perhaps this depression and the *MI* indentation are connected as a single geologic entity; however, because of our images' N/S ambiguity, any inferences about structural attributes normal to the equatorial plane are necessarily tentative.

Another interesting feature, seen at both low and high resolution just above the *MI* indentation in frame 8, is a tiny bright glint that probably arises from part of the indentation's interior that fortuitously faces the radar in a narrow phase interval. A candidate crater is just

to its left. In frames 9-12 of Fig. 1 lc, to the left of and slightly lower than the *ml* indentation, is a small dark feature that looks like an oblong concavity and may be two adjacent craters. This feature is also seen at lower resolution in Fig. 9.

Other candidates for craters are seen lower down in frame 12 and just below the *ml* tip in frame 1. The dark blotch above the *m2* tip in frame 7 of Fig. 9 becomes mottled at high resolution; some of its structure repeats in frames 4- 8 and may be craters on the verge of being resolved. More definitive statements about the topography responsible for all these features may follow from development of a 3-D shape model and concurrent refinement of the orbit.

Strange Ends

The silhouette's ends are morphologically striking and possess a subtle, almost pinwheel-like symmetry. Each tip consists of a rounded knob whose radius of curvature is only a few hundred meters. Up from the *m2* tip (toward the COM), the leading (left) side of the silhouette is gently curved and convex, whereas the trailing (right) side is concave, giving the tip an almost hooklike appearance. A more subdued concavity on the trailing (left) side of the *ml* end is perceptible in Fig. 11. Back from the shallow concavities that define the "hooks," the trailing sides of the silhouette are nearly linear for a kilometer.

The peculiar morphology of *Geographos*' ends maybe related to the pattern of ejects removal and deposition caused by the combination of the asteroid's gravity field and rotation. Burns (1975) compared effects of gravitational and centrifugal accelerations for slightly nonspherical asteroids and concluded that asteroid regoliths general 1 y are gravitational y bound. However, he noted that even if particles at the tip of the body were gravitationally bound, "there might be small protuberances on the surface where [centrifugal acceleration

exceeds gravitational attraction]. Since the gravitational force is a long-range force, in general this is unlikely although very unusual surface shapes might be kept clean by centrifugal effects. ” Staley (1970) worried that “in the case of a pointed, cigar-shaped Geographos, . . . a man, unless tethered to the surface, could indeed be lost in space,” but his calculations assumed an elongation of 4.4.

Scheeres (1994) presented a general formulation of the orbital dynamics around uniform-density, uniformly rotating triaxial ellipsoids, and Scheeres *et al.* (1994) used a radar-based model of Castalia (Hudson and Ostro 1994) to study close orbits around that body. With an accurate three-dimensional model of Geographos, it would be possible to estimate the local force gradient at any point on the asteroid (Dobrovolskis and Burns, 1980; Thomas *et al.*, 1993), thereby obtaining an initial indication of the ability of the surface to retain loose particles. It also would be possible to compute local bounds on impact ejects launch velocities that lead either to retention in the vicinity of the impact or to escape from the asteroid (Scheeres *et al.*, 1994). Finally, a study of the dynamics of close orbits would let us identify sites on the surface where ejects may preferentially accumulate (Dobrovolskis and Burns, 1980; Geissler *et al.*, 1994) and would let us estimate the returning fraction of ejects as a function of launch velocity. These analyses may elucidate the nature and origin of the asteroid’s ends.

Surface Characteristics

Geographos presumably is the cumulative product of a sequence of collisions, perhaps originating in disruption of a very much larger parent body and proceeding through an interval of relatively low-energy impacts. If we knew the thickness of the regolith, the set of possibilities for formation/evolution scenarios would be narrowed. What can Geographos’

radar properties tell us about regolith characteristics? The lack of sharp angularity in the silhouette and the rarity of prominent brightness variations in the images suggest that topography is more subdued than might be expected for a freshly formed fragment or a recent victim of a nearly catastrophic collision. However, what should be expected for such entities is not clear to us. Similarly, one might interpret the asteroid's modest roughness at cm-to-m scales as indicating a regolith at least several decimeters deep, but such an inference concatenates assumptions about ejecta production and retention, the surface's mechanical response to impact, etc., that may be wrong.

A useful constraint on inferences about Geographos' regolith is the OC radar albedo,

$$\hat{\sigma}_{\text{OC}} = \sigma_{\text{OC}} / A_{\text{proj}}, \quad (3)$$

where A_{proj} is the target's projected area. For an object with negligible SC echo, $\hat{\sigma}_{\text{OC}}$ is a first approximation to the product of the surface's normal reflectance R and a gain factor g that depends on target shape and orientation. R constrains surface bulk density d , and an empirical relation (Garvin *et al.* 1985) applicable here is

$$d(R) = 3.2 \ln \left[\frac{1 + \sqrt{R}}{1 - \sqrt{R}} \right] \quad (4)$$

The gain factor would be unity for a sphere, and larger (or smaller) than unity for a shape whose distribution of projected surface area with incidence angle weights normally oriented area more (or less) heavily than a sphere. We don't yet know Geographos' three-dimensional shape. If it were an ellipsoid with axes $2a = 5.11$ km, $2b = 1.85$ km, and $2c = 1.5$ km, then the radar albedo would be about 0.13. If the rotational coverage averaged out departures of g from unity, then we would calculate a density about 2.4 g cm^{-3}

Interpretations of Geographos' visible/infrared reflectance spectra seem to favor a stony-iron mineralogy over an ordinary chondritic one (Hicks *et al.* 1995, Clark *et al.* 1995). The corresponding porosities for candidate meteoritic analogs to S asteroids range from about 30% for ordinary chondrites to about 50% for stony irons, that is, in the realm of typical values for the lunar regolith. Our assumption that all the OC echo power is from single backreflections from smooth sulfate elements may have led to over-estimation of d and under-estimation of porosity; however, the simplistic assumption about shape (and hence g) is the primary source of uncertainty (Ostro *et al.* 1991 b).

Herein lies yet another motivation for using the delay-Doppler images to estimate the asteroid's three-dimensional shape: the modeling can decouple effects of surface curvature from scattering properties, thereby eliminating bias in estimation of R and d . Because of Goldstone's equatorial view of Geographos, unambiguous shape reconstruction will rely on non-equatorial lightcurves to break the radar images' N/S ambiguity. The inversion is expected to elucidate the detailed three-dimensional character of the surface at ~ 100-m scales, including its polar extent and the geologic nature of features in the images. It also will improve substantially upon both the E-34 orbit and the co-registration of images from multiday sums.

ACKNOWLEDGMENTS

We thank the Goldstone technical staff for their support of these observations and Per Magnusson for providing us with up-to-date information about lightcurve-based constraints on Geographos' spin vector. This research was conducted at the Jet Propulsion Laboratory, California Institute of Technology, under contract with the National Aeronautics and Space Administration (NASA), and at Washington State University.

REFERENCES

- BURNS, J. A. 1975. The angular momenta of solar system bodies: implications for asteroid strengths. *Icarus* **25**, 545-554.
- CHAPMAN, C. R., D. MORRISON, AND B. ZEILNER 1975. Surface properties of asteroids: A synthesis of polarimetry, radiometry, and spectrophotometry. *Icarus* **25**, 104-130.
- CLARK, R. E., J. F. BELL, F. P. FANALE, AND D. J. O'CONNOR 1995. Results of the seven-color asteroid survey: Infrared spectral observations of ~50-km size S-, K-, and M-type asteroids. *Icarus* **113**, 387-402.
- DOBROVOLSKIS, A. R., AND J. A. BURNS 1980. Life near the Roche limit: Behavior of ejecta from satellites close to planets. *Icarus* **42**, 422-441.
- DUNLAP, J. L. 1972. *Laboratory Work on the Shape of Asteroids*. M.S. Thesis, Univ. of Arizona, Tucson,
- DUNLAP, J. L. 1974. Minor planets and related objects. XV. Asteroid (1620) Geographos. *Astron. J.* **79**, 324-332.
- GAFFEY, M. J., J. F. BELL, R. H. BROWN, J. L. PIATEK, K. L. REED, AND D. A. CHAKY 1993. Mineralogic variations within the S-type asteroid class. *Icarus* **106**, 573-604.
- GARVIN, J. B., J. W. HEAD, G. H. PETTINGILL, AND S. H. ZISK 1985. Venus global radar reflectivity and correlations with elevation. *J. Geophys. Res.* **90**, 6859-6871.
- GEISSLER, P. E., J.-M. PIETT, R. GREENBERG, W. BOTKE, M. NOLAN, AND D. DURDA 1994. Erosion and regolith Redistribution on 243 Ida and its moon (abstract). *Bull. Amer. Astron. Soc.* **26**, 1157.
- HICKS, M., W. GRUNDY, U. FINK, S. MOTTOLA, AND G. NEUKUM 1995. Rotationally resolved spectra of 1620 Geographos. *Icarus* **113**, 456-459.

- HUDSON, R. S. 1993. Three-dimensional reconstruction of asteroids from radar observations. *Remote Sensing Reviews* **8**, 195-203.
- HUDSON, R. S., AND S. J. OSTRO 1994. Shape of asteroid 4769 Castalia (1989PB) from inversion of radar images. *Science* **263**, 940-943.
- KWIATKOWSKI, T. 1995. Sidereal period, pole, and shape of asteroid 1620 Geographos. *Astron. Astroph.* **294**, 274-277.
- P. MAGNUSSON, M. DAHLGREN, M. A. BARUCCI, L. JORDA, R. P. BINZEL, S. M. SIVAN, C. BLANCO, D. RUCCIOLI, B. J. BURATTI, F. COIAS, J. BERTHIER, G. DE ANGELIS, M. DIMARTINO, E. DOTTO, J. D. DRUMMOND, U. FINK, M. HICKS, W. GRUNDY, W. WISNIEWSKI, N. M. GAFTONYUK, E. H. GEYER, T. BAUER, M. HOFFMAN, V. IVANOVA, B. KOMITOV, Z. DONCHIEV, P. DENCHEV, YU. N. KRUGLY, F. P. VELICHKO, V. G. CHIORNY, D. F. LUPISHKO, V. G. SHEVCHENKO, T. KWIATKOWSKI, A. KRYSZCZYNSKA, J. F. LAHULLA, J. LICANDRO, O. MENDEZ, S. MOTTOLA, A. ERIKSON, S. J. OSTRO, P. PRAVEC, W. PYCH, D. J. THOLEN, R. WHITELEY, W. J. WILD, M. WOLF, AND L. ŠAROUNOVÁ 1995. Photometric observations and modeling of asteroid 1620 Geographos. Submitted for publication.
- NOZETTE, S., AND H. B. GARRETT 1994. Mission offers a new look at the Moon and a near-Earth asteroid. *Eos, Trans., Amer. Geophys. Union* **75**, No. 14, 161.
- OSTRO, S. J. 1993. Planetary radar astronomy. *Rev. Modern Physics* **65**, 1235-1279.
- OSTRO, S. J., R. CONNELLY, AND L. BELKORA 1988. Asteroid shapes from radar echo spectra: A new theoretical approach. *Icarus* **73**, 15-24.
- OSTRO, S. J., J. F. CHANDLER, A. A. HINE, K. D. ROSEMA, I. I. SHAPIRO, AND D. K. YEOMANS 1990a. Radar images of asteroid 1989 PB. *Science* **248**, 1523-1528.
- OSTRO, S. J., K. D. ROSEMA, AND R. F. JURGENS 1990b. The shape of Eros. *Icarus* **84**, 334-351.

- OSTRO, S. J., D. B. CAMPBELL, J. F. CHANDLER, I. I. SHAPIRO, A. A. HINE, R. VEJIZ, R. F. JURGENS, K. D. ROSEMA, R. WINKLER, AND D. K. YEOMANS 1991a. Asteroid radar astrometry. *Astron. J.* **102**, 1490-1502.
- OSTRO, S. J., D. B. CAMPBELL, J. F. CHANDLER, A. A. HINE, R. S. HUDSON, K. D. ROSEMA, AND I. I. SHAPIRO 1991 b. Asteroid 1986 DA: Radar evidence for a metallic composition. *Science* 252, 1399-1404.
- OSTRO, S. J., D. B. CAMPBELL, R. A. SIMPSON, R. S. HUDSON, J. F. CHANDLER, K. D. ROSEMA, I. I. SHAPIRO, E. M. STANDISH, R. WINKLER, D. K. YEOMANS, R. VEJIZ, AND R. M. GOLDSTEIN 1992. Europa, Ganymede, and Callisto: New radar results from Arecibo and Goldstone. *J. Geophys. Res.* 97, 18,227-18,244.
- OSTRO, S. J., K. D. ROSEMA, R. S. HUDSON, R. F. JURGENS, J. D. GIORGINI, R. WINKLER, D. K. YEOMANS, D. CHOATE, R. ROSE, M. A. SIADAT, S. D. HOWARD, AND D. L. MITCHELL 1995. Extreme elongation of asteroid 1620 Geographos from radar images. *Nature* 375,474-477 (1995).
- PRIEST, P. 1993. *Goldstone Solar System Radar Capability and Performance* (Jet Propulsion Laboratory, Pasadena, CA) Internal Report 1740-4.
- SCHIFFERIS, D. J. 1994. Dynamics about uniformly rotating triaxial ellipsoids: Applications to asteroids. *Icarus* 110, 225-238.
- SCHIFFERIS, D. J., S. J. OSTRO, R. S. HUDSON, AND R. A. WERNER 1994. Orbits about asteroid 4769 Castalia (abstract). *Bull. Amer. Astron. Soc.* 26, 1166-1167.
- STALEY, D. O. 1970. Man on an asteroid. *J. Geophys. Res.* 75,5571-5573.
- THOMAS, P. C., J. VEVERKA, D. SIMONELLI, P. HELFENSTEIN, P. B. CARCICH, M. J. S. BELTON, M. E. DAVIES, AND C. CHAPMAN 1993. The shape of Gaspra. *Icarus* 107,23-36.
- VEJIZ, R. G. J., M. S. HANNER, D. L. MATSON, E. F. TEDESCO, I. A. LEBOWSKY, AND A. T. TOKUNAGA 1989. Radiometry of near-Earth asteroids. *Astron. J.* 97, 1211-1219.

TABLE I
Geographos Ephemeris and Goldstone Transmit Windows^a

DOY	Date	UTC Transmit Window		RA	Dec	RTT (s)	Predicted SNR	
		start	stop					
		hh:mm-hh:mm	h				/date	max/run
240	Aug 28	05:50-08:15	2.4	321.3°	-38°	39	790	135
241	Aug 29	04:15-09:25	5.1	321.5°	-30°	46	1400	115
242	Aug 30	04:25-10:00	5.5	321.6°	-23°	48	1100	90
243	Aug 31	03:37-10:10	6.5	321.7°	-18°	53	900	69
244	Sep 1	03:10-10:25	7.2	321.8°	-14°	59	680	53
245	Sep 2	02:50-10:15	7.4	321.9°	-10°	65	490	38
246	Sep 3	02:35-10:20	7.7	321.9°	-7°	71	330	27

^aDOY is day of year, RA is right ascension, Dec is declination, and RTT is echo roundtrip time delay (approximately equal to the distance in 10^{-3} AU). Predicted values of the signal-to-rms-noise ratio (SNR) per date and the maximum SNR per run were based on conservative assumptions about the target and the radar system.

TABLE 11

Setups^a

Baud (Al)	RP	NCOH	BAND	Δf	NL	col, row
7.000 μ s	889.000 μ s	1	1124.9 Hz	17.6 Hz	70	23, 11
(1050 m)	(133.335 km)		(59.4 km)	(0.93 km)		
7.125 μ s	904.875 μ s	1	1105.1 Hz	17.3 Hz	70	23, 11
(1069 m)	(135.731 km)		(58.3 km)	(0.91 km)		
1.000 μ s	1277.000 μ s	43	183.12 Hz	2.8612 Hz	11	16, 12
(150 m)	(19.050 km)		(9.7 km)	(0.151 km)		
0.500 μ s	63.500 μ s	150	104.99 Hz	1.6404 Hz	9	32, 16
(75 m)	(9.525 km)		(5.54 km)	(0.087 km)		
CW			500.00 Hz	1.9531 Hz	96	128

^aEach setup's time resolution (baud, Δt), code repetition period RI), unaliased frequency window BAND, and frequency resolution Δf are given, along with their length equivalents (see text). NCOH is the number of RP-long time series of voltage samples coherently summed after decoding. Fourier analysis of an RP-long time series of voltages within any given range cell produces a power spectrum, and repetition of that process for each range bin produces a delay-Doppler image that is referred to as one look. The number of looks summed to produce a single data record is given in the column labeled NL. The last two columns list the offset from (0,0) in the recorded power arrays that would contain echoes from a point target if the delay-Doppler ephemeris were perfect.

TABLE III
Overview of Geographos Observations^a

File	Baud (μ s)	Receiving Sys, Poln.	Run Stats, Sequence	Run UTC Interval	Phase Interval	'tint (s)
Aug. 28 (DOY 240)						
ge005	7.0	1 OC	8/ 8 (1- 8)	0618-0632	301-316	27.9
ge006	7.125	1 OC	3/ 3 (9- 11)	0658-0702	34-1-351	33.8
ge007	1.0	1 Oc	17/19 (12- 30)	0711-0744	2- 43	18.8
ge008	1.0	1 OC	12/12 (31- 42)	0753-0815	50- 75	19.7
Aug. 29 (DOY 241)						
ge103	1.0	1 OC	11/11 (1- 11)	0436-0454	45- 68	23.1
ge104	1.0	1 Oc	46/46 (12- 56)	0513-0647	87-196	23.6
ge105	1.0	1 Oc	35/35 (57- 91)	0655--0803	205--283	23.5
ge106	1.0	1 Oc	27/29 (92-120)	0810-0923	292- 15	22.8
Aug. 30 (DOY 242)						
ge203	1.0	1 Oc	3/ 4 (1- 4)	0444/-0502	290-294	30.8
ge205	0.5	1 Oc	3/ 3 (5- 7)	0515-0520	310-315	21.9
ge206	0.5	1 Oc	43/49 (8- 56)	0523-0707	320- 64	21.9
ge207	0.5	1 Oc	50/51 (51-107)	0713-0902	86-211	21.9
ge208	0.5	1 Oc	27/27 (108-134)	0904/-1001	218-279	21.9
Aug. 31 (DOY 243)						
ge303	0.5	1 Oc	21/21 (1- 21)	0339-0430	59-120	32.8
ge307	0.5	2 Oc	52/52 (27- 78)	0543-0728	207- 322	32.9

ge308	0.5	2	Oc	54/54	(79-133)	0738- 0927	335- 99	32.9
ge309	1.0	2	SC	3/ 3	(134-136)	0940-0944	114-119	37.2
<i>9C310</i>	1.0	2	OC	2/ 2	(137-138)	0946-0949	122- 125	42.3
ge311	1.0	2	SC	9/ 9	(139-147)	0952-1000	128- 137	35.5
Sep , 1 (DOY 244)								
ge409	7.0	2	Oc	3/ 3	(22- 24)	0654-0700	142- 148	45.1
ge410	7.0	2	OC	4/ 4	(25-- 28)	0- /02 -0 "/10	152-160	47.8
ge411	7.0	2	Sc	38/38	(29- 66)	0713-0841	163-264	46.4
ge412	"/.0	2	SC	32/33	(61- 99)	0907- 1025	282-371	47.4
Sep, 2 (DOY 245)								
ge245a	cw	1	OC/SC	61/61	(1- 61)	0354- 0630	154-328	32.4
ge245b	c w	1	OC/SC	77/82	(62-143)	0648-1016	353-230	32.2

^aInformation is given for individual data files. The first digit in the file name is the same as the last digit in the day of year (DOY). The baud, or delay-resolution (Δt), identifies the setup from Table 11. The receiving antenna was DSS - 14. We used either the two-horn (subreflector/maser) system or the single-horn/hemt system, as described in the text. SC is the same circular polarization as transmitted and OC is the opposite circular. Under *Run Statistics*, the number of useful runs is followed by a slash and the total number of runs. Runs on each date were numbered from 1; the table lists the run sequence contained in each file, the corresponding UTC interval spanned, and the average run integration time (Δt_{int}). We used ephemeris E-18 during Aug. 28-30 and E-22 during Aug. 31 - Sep. 3.

TABLE IV
Corrections to Delay-Doppler Ephemerides from 1- μ s Images

Date	Epoch (hh:mm:ss)	Model	Corrections	
			Delay (μ s)	Doppler (Hz)
Aug. 28	07:10:00	2D	71.820	-2.58
		3D	--73.583	-3.49
		(2D + 3D)/2	--72.702	-3.14
		2D - 3D	1.763	0.91
Aug. 29	04:40:00	2D	-49.947	-2.00
		3D	-51.076	-2.17
		(2D + 3D)/2	-50.512	-2.10
		2D - 3D	1.129	0.17

TABLE V

Goldstone 8S1O-MIIZ Radar Astrometry Referenced to Geographos' Center of Mass^a

UTC epoch of echo reception	Time delay (UTC μ s)	Estimate	Residual	Doppler frequency (Hz)	Estimate	Residual
1994 08 2807:10	38936537.06 \pm 1.76	-0.91		-364880.6 \pm 0.9	-0.7	
1994 08 2904:40	42596456.40 \pm 1.13	0.33		-427851.0 \pm 0.2	-0.1	
1994 09 0207:20	615553.2 \pm 0.5	0.1				

^aResiduals are with respect to ephemeris B-34 (see text).

TABLE VI
Geographos Orbit ((1 OD-34)^a

Epoch	1994 Sep. 5.0 (TDB)
Eccentricity	0.335548231 (39)
Perihelion Distance (AU)	0.827592428 (48)
Perihelion Passage (TDB)	1994 June 76.8433836 (62)
Argument of Perihelion (deg.)	2°/6.7218589 (135)
Longitude of Ascending Node (deg.)	337.3708609 (112)
Inclination (deg.)	13.3421674 (184)

^aThese orbital elements result from a fit to optical and radar observations over the interval from 1951 Aug. 31 to 1994 Sept. 2. A total of 760 optical astrometric observations were processed. The employed radar data included 3 Doppler and 2 delay observations in Table V and one Doppler and one delay observation made in February 1983 (Ostro *et al.* 1991a). We used JPL planetary ephemeris DE-245 (J2000). The rms residual for all 760 optical observations is 0.89 arc seconds and the 1994 radar rms residuals are 0.1 Hz and 0.3 μ s. The angular orbital elements are referred to the mean ecliptic and equinox of J2000 and the 3-sigma formal uncertainties (in parentheses) are given in units of the last decimal place.

FIGURE CAPTIONS

1. Block diagram of the Goldstone radar system (Priest 1993). The signal path can be outlined as follows. A range code or a frequency-hopped cw signal is sent to the exciter, where it modulates the 8510-MHz carrier. The output signal is amplified by the klystrons to about 470 kW and transmitted. Echoes are amplified, demodulated to a 7.5-MHz intermediate-frequency (IF) signal, and passed to complex mixers for conversion to baseband in-phase and quadrature (I and Q) signals. For cw observations, the baseband signals are low-pass filtered, sampled at 2 kHz, and passed to an IBM 386 computer, which forms power spectra and writes them to disc. For phase-coded observations, which are controlled by the VAX 11/780 computer, baseband signals are sampled at 40 MHz, digitally filtered in baud integrators, and demodulated by correlation against the range code. The array processor puts data from the correlators and accumulators into floating-point format and spectral analysis of decoded voltages produces delay-Doppler power arrays, which are recorded on disc and are simultaneously displayed in real time on a Macintosh II computer. At convenient intervals, data files on the VAX or the IBM are transferred to a Sun IPX workstation for processing.

2. Spectra from the Sep. 2 cw observations (Table 11.1), smoothed to 6-Hz resolution. Echo power in the OC (solid curves) and SC (dotted curves) polarizations is plotted vs. Doppler frequency in a 300-Hz window centered on 0 Hz. Identical linear scales are used throughout the figure. Labels give rotation phase.

3. Weighted sum of all 138 spectra from the Sep. 2 cw observations (Fig. 2). OC (solid curve) and SC (dotted curve) echo power is plotted vs. Doppler frequency.

4. OC, SC and total-power ($TC=OC+SC$) radar cross sections from the cw spectra (Fig. 2), plotted vs. rotation phase.

S. Estimates of circular polarization ratio ($\mu_c = SC/OC$) from the cw spectra (Fig. 2), plotted vs. rotation phase. The faint curves define the ± 1 -standard-deviation error interval.

6. (a) The white curve is our cw estimate of the hull on Geographos' pole-on silhouette and the X marks the projected position of the asteroid's center of mass (COM) with respect to the hull. The curve and the X are superposed on the Aug. 30 estimate of the silhouette itself from 0.5- μ s images (Ostro *et al.* 1995); the bright pixel is the projection of the COM determined from analysis of those images. The absolute scales and relative rotational orientations of the two figures are known. If there were no errors in any of the estimations, then positioning the X on top of the bright pixel would co-register the hull and the silhouette, that is, would make the hull look wrapped around the silhouette. We wish to compare the shapes of the hull and the silhouette and therefore have adjusted the relative positions of the two figures to co-register the hull with the silhouette. The resultant offset between the X and the bright pixel is a measure of the uncertainty in our knowledge of the COM's delay-Doppler trajectory during the experiment. Note that the wrapping of the hull around the silhouette's *MI* side is a bit too loose, that is, it is bowed out instead of straight, apparently due to our Fourier series truncation (Ostro *et al.* 1988). The silhouette's extreme breadths, 5.11 ± 0.11 km and 1.85 ± 0.11 km, are in a ratio = 2.76 ± 0.18 (Ostro *et al.* 1995). (b) Quantities associated with the hull estimation, in units of kilometers vs. rotation phase (degrees), Black dots with error bars are support function data, p_{dat} . Superposed on those data is a white curve corresponding to the constrained Fourier-model mean. The black curve on top of that white curve is the unconstrained Fourier model p_{unc} . The dashed curve at the top of the figure is the hull's bandwidth, $p_{con}(0) + p_{con}(0+180^\circ)$, and the solid curve at the bottom of the figure is the hull's middle-frequency, $[p_{con}(0) - p_{con}(0+180^\circ)]/2$.

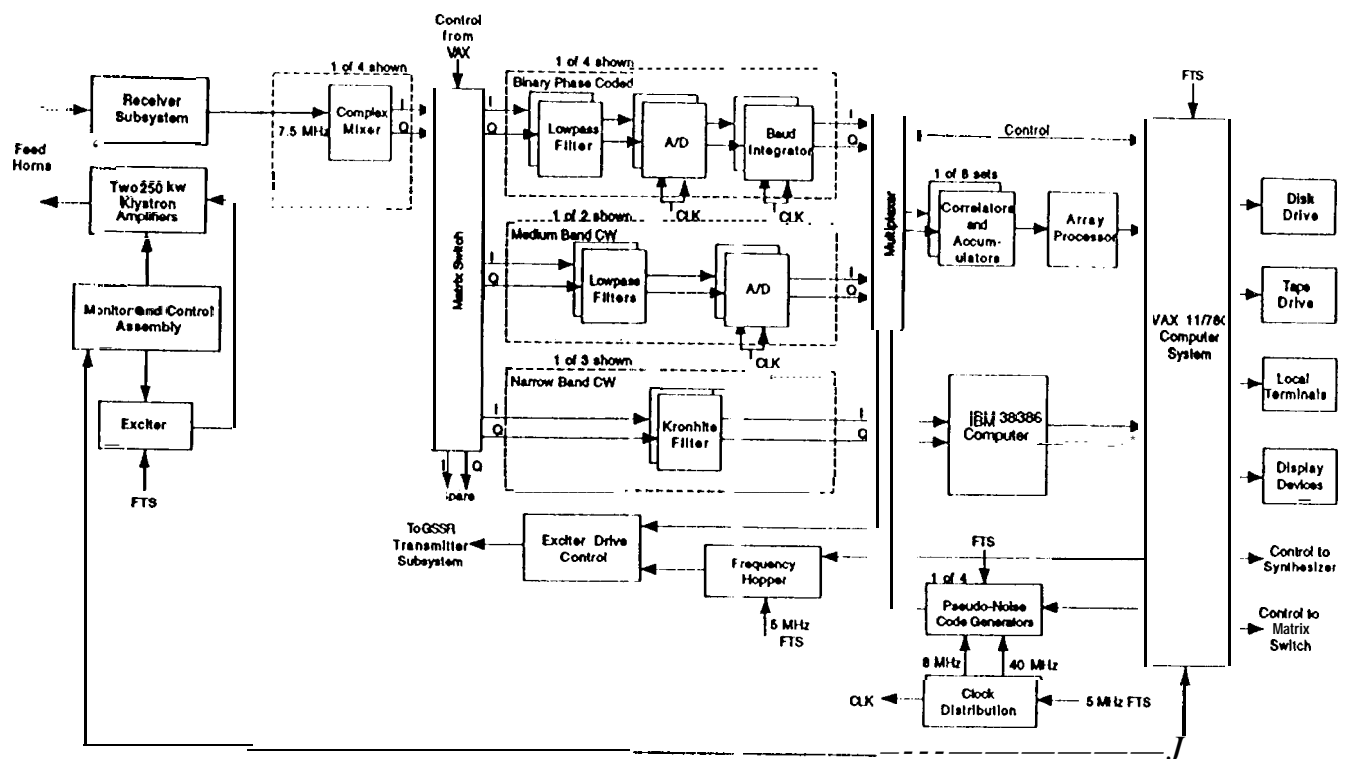
7. Echo spectra at phases corresponding to bandwidth extrema. OC (solid curve) and SC (dotted curve) echo power is plotted vs. Doppler frequency.

8. Geographos low-resolution radar movie. **(a)** Phase of single-run images and file identifications from Table III. **(b)** 150 single-run images from observations with the $1.0 \mu\text{s} \times 2.86 \text{ Hz}$ ($150 \times 151 \text{ m}$) setup are shown in chronological order from left to right in the top row, etc. The radar is toward the top, time delay (range) increases toward the bottom, and Doppler frequency (radial velocity) increases toward the left.

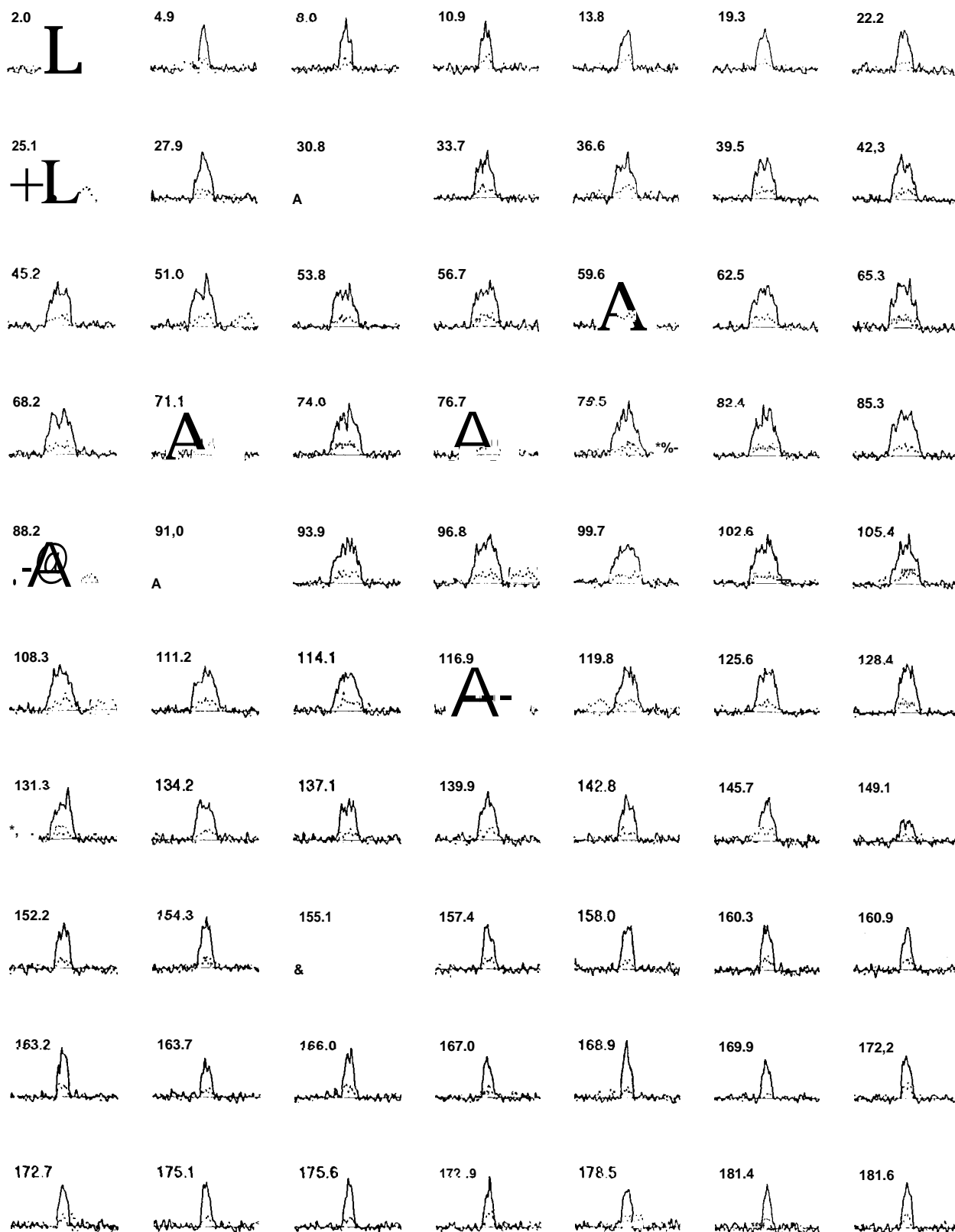
9. Multi-run sums of low-resolution images within twelve independent, 300-wide rotation-phase blocks. In the top row, the asteroid-to-radar vector points toward 12 o'clock in the far left image, toward 11 o'clock in the next image, etc. The resolution is $1.0 \mu\text{s} \times 2.86 \text{ Hz}$ ($150 \times 151 \text{ m}$).

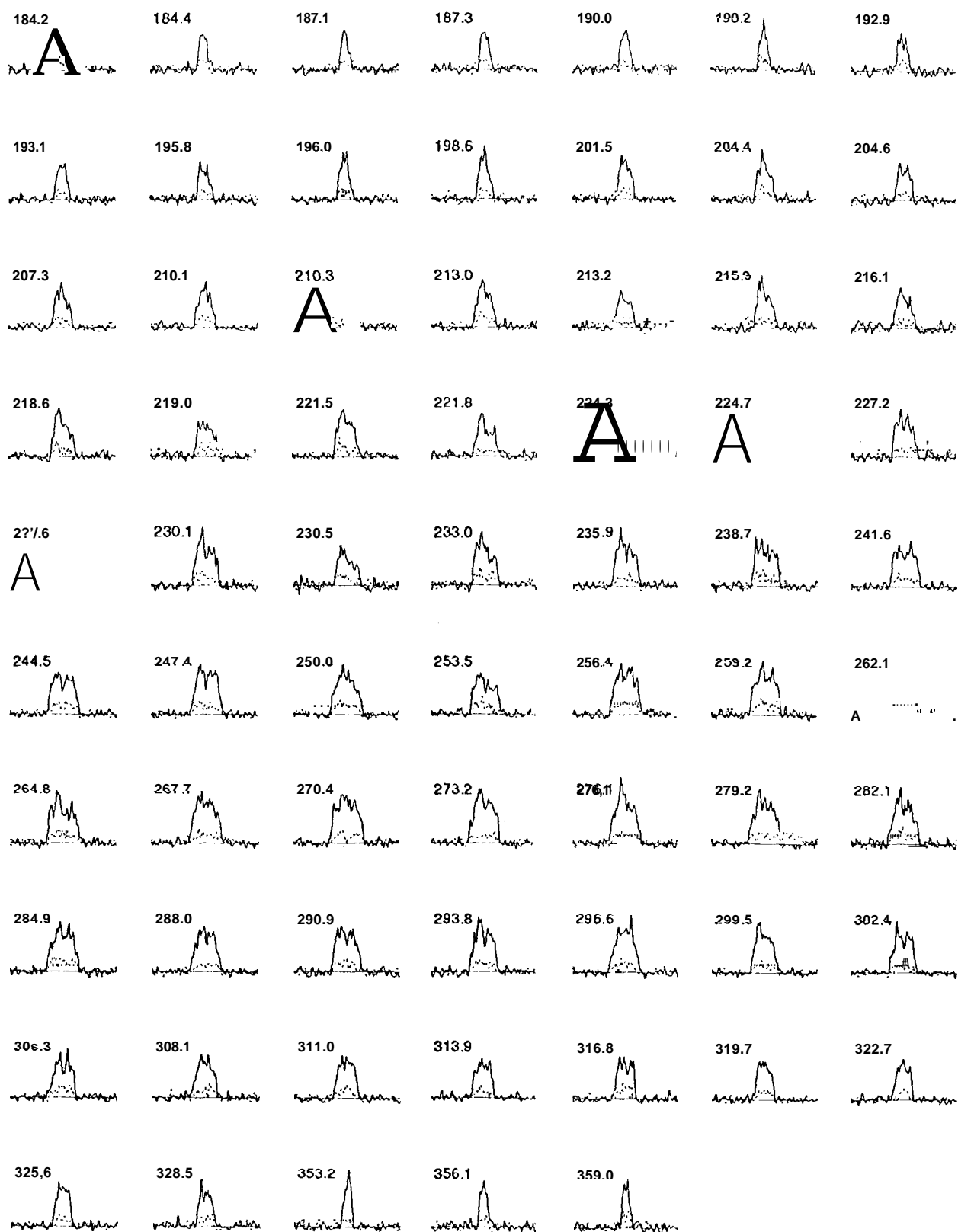
10. Geographos high-resolution radar movie. **(a)** Phase of single-run images and file identifications from Table III. **(b)** 250 single-run images from observations with the $0.5 \mu\text{s} \times 1.64 \text{ Hz}$ ($75 \text{ m} \times 87 \text{ m}$) setup are shown in chronological order from left to right in the top row, etc. The radar is toward the top, time delay (range) increases toward the bottom, and Doppler frequency (radial velocity) increases toward the left.

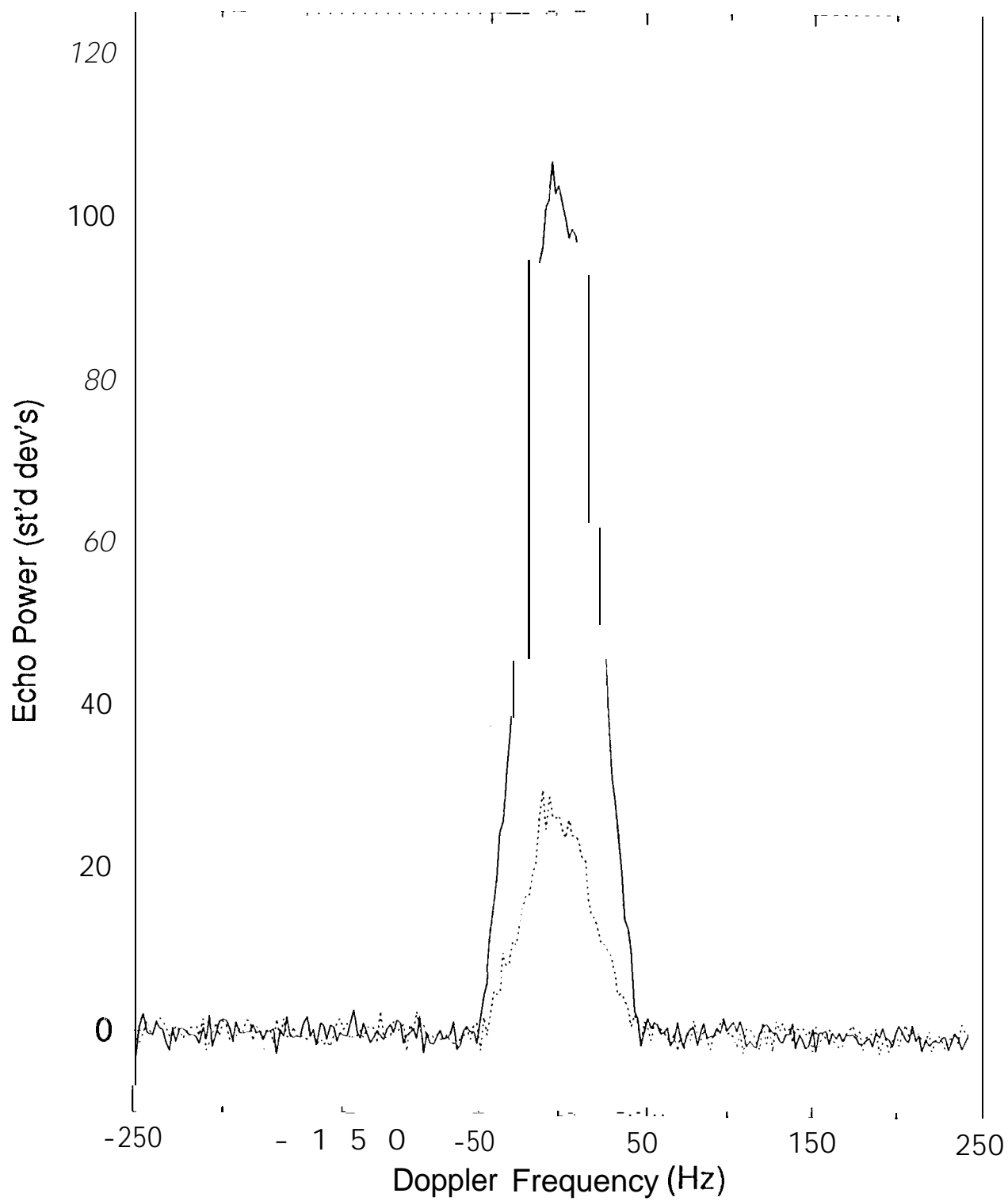
11. Multi-run sums of high-resolution images within twelve independent, 300-wide rotation-phase blocks, from **(a)** Aug. 30, **(b)** Aug. 31, and **(c)** both dates. In the top rows of (a), (b), and (c), the asteroid-to-radar vector points toward 12 o'clock in the far left image, toward 11 o'clock in the next image, etc. The resolution is $0.5 \mu\text{s} \times 1.64 \text{ Hz}$ ($75 \text{ m} \times 87 \text{ m}$).



Ostro et al. Fig. 1

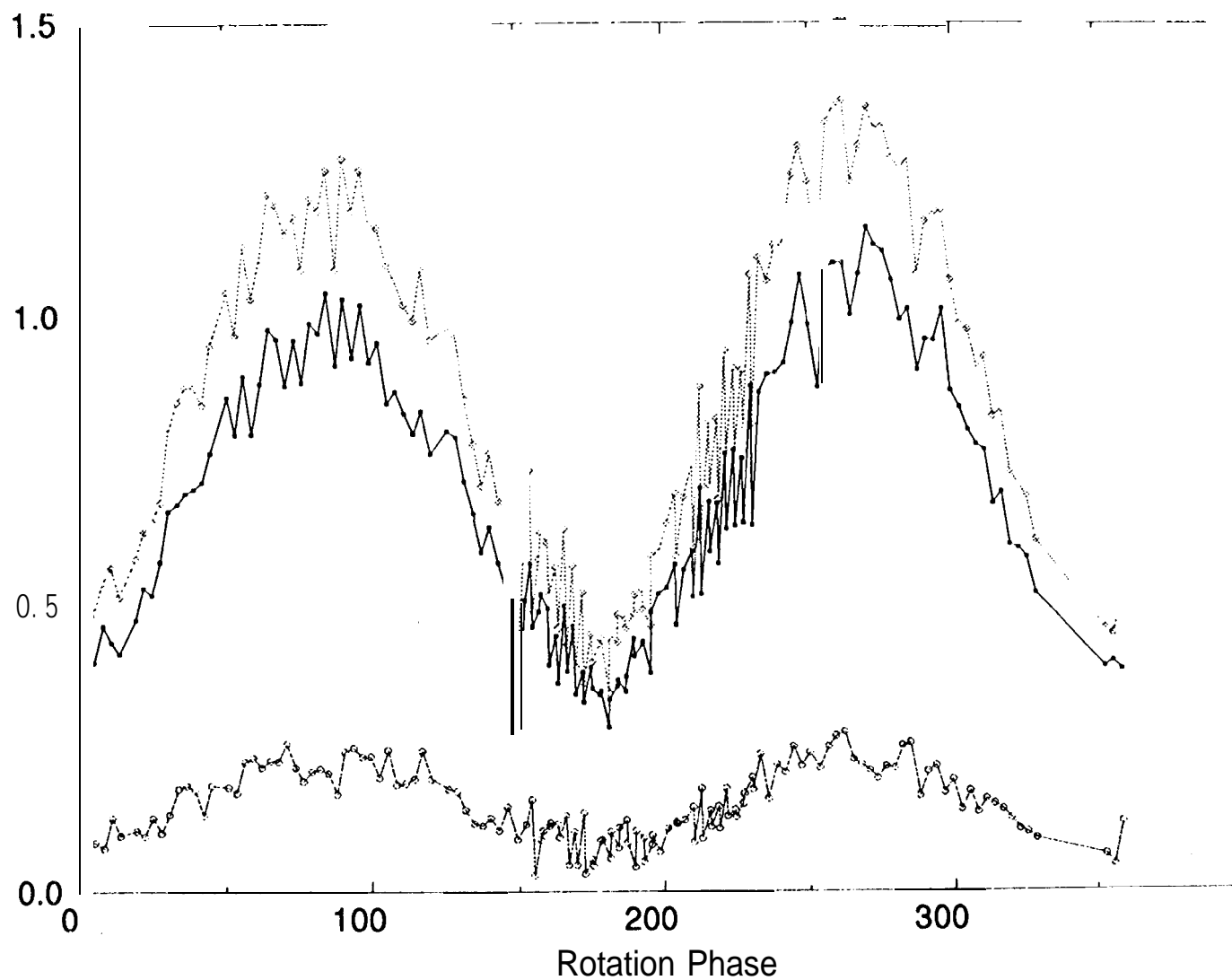




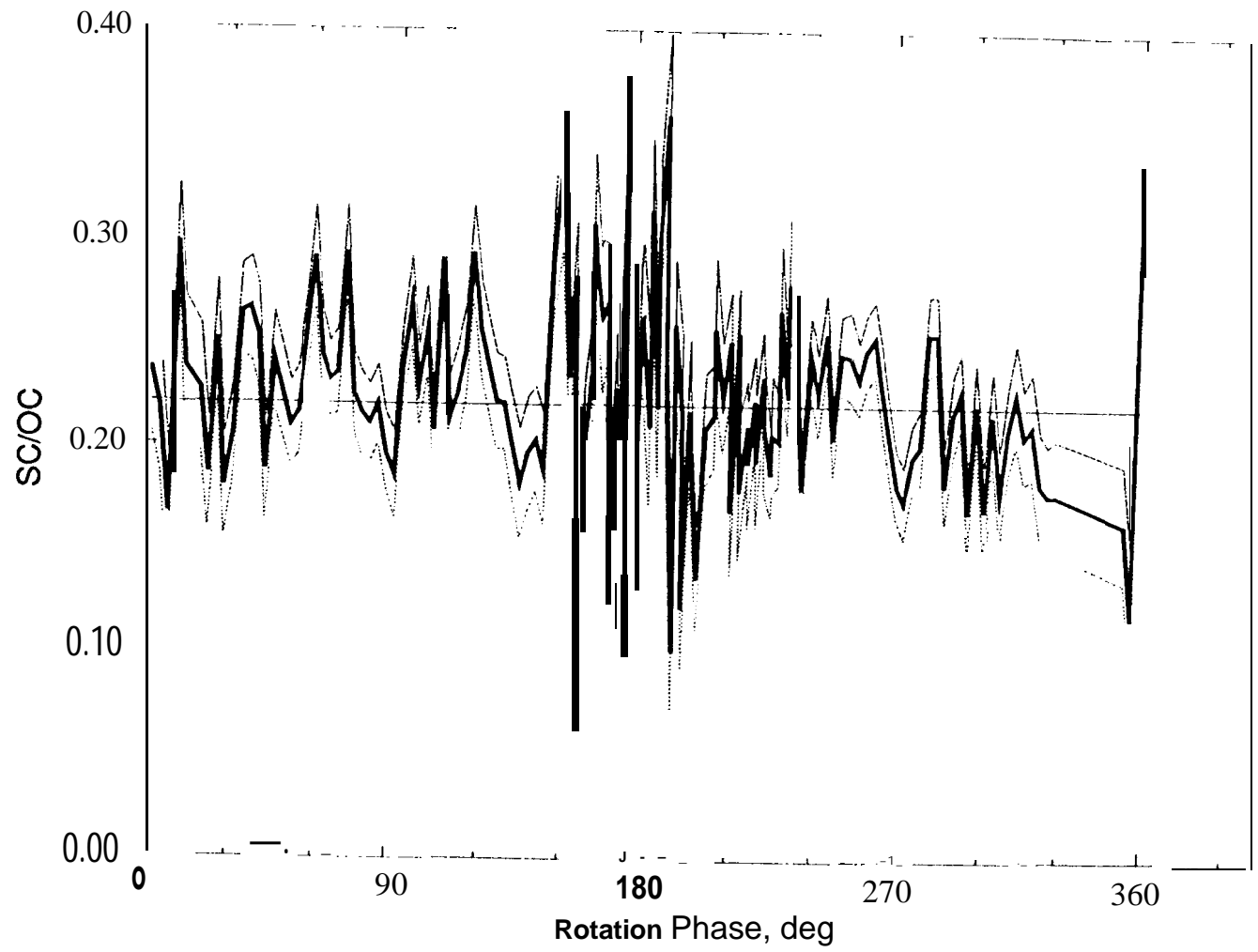


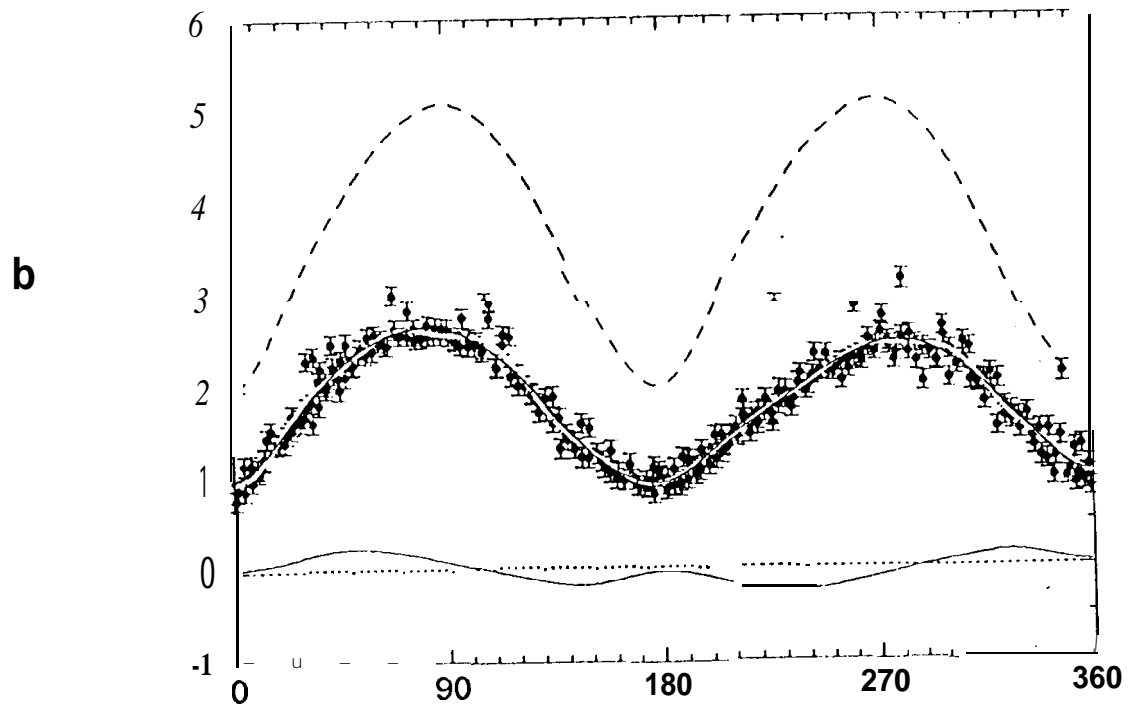
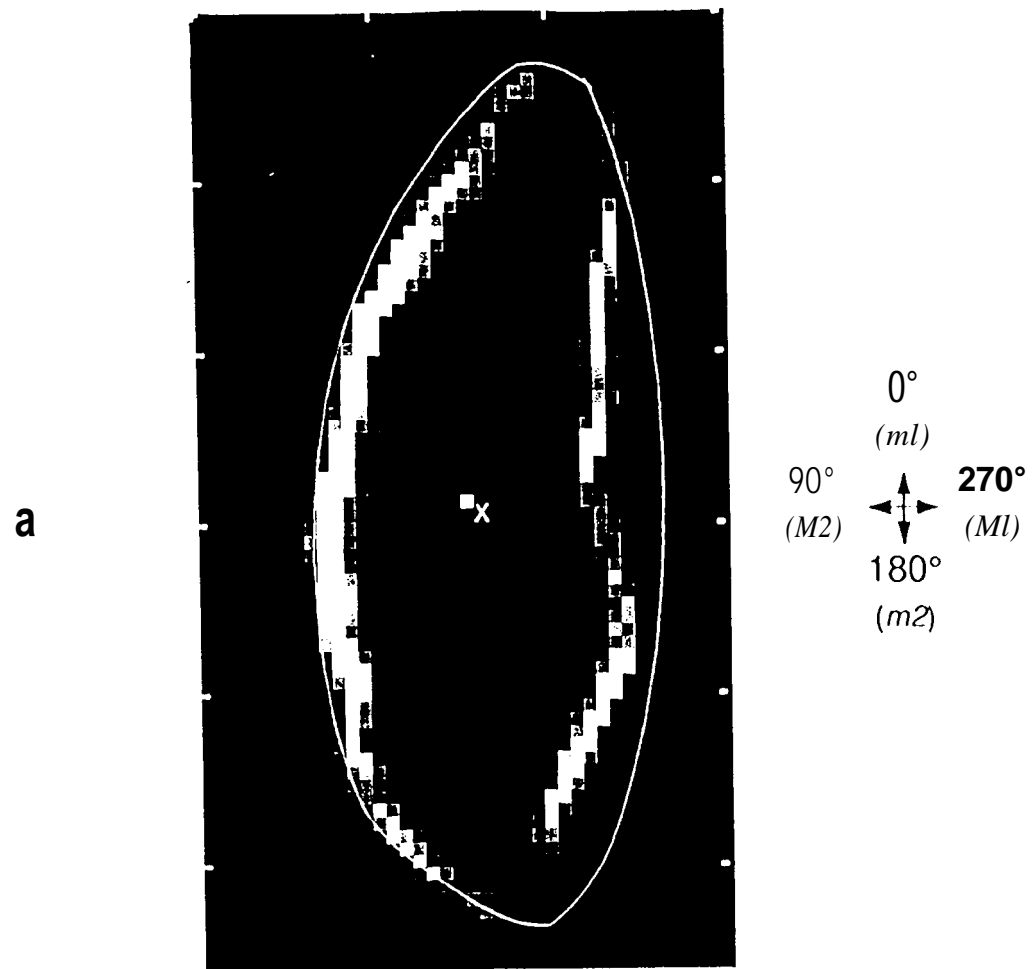
Ostro *et al.* Fig. 3

Geographos OC, SC, TC cross sections

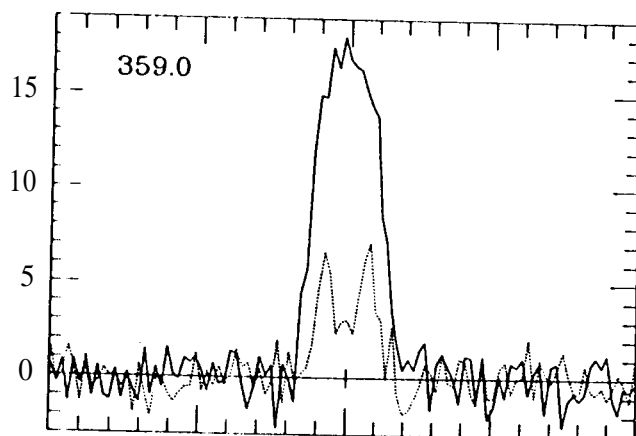
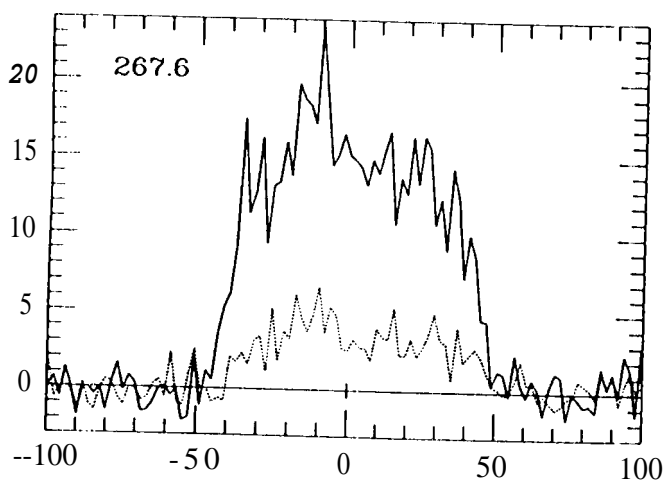
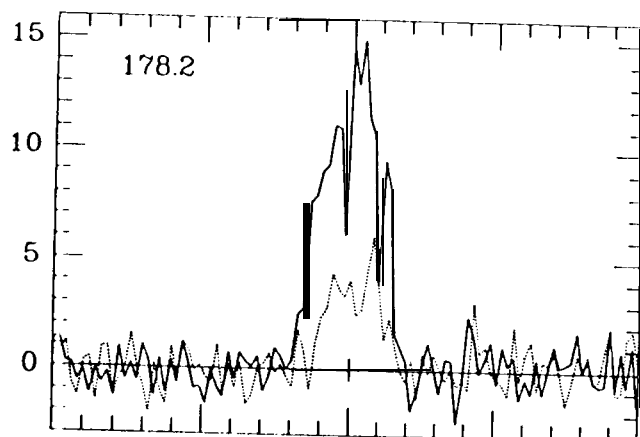
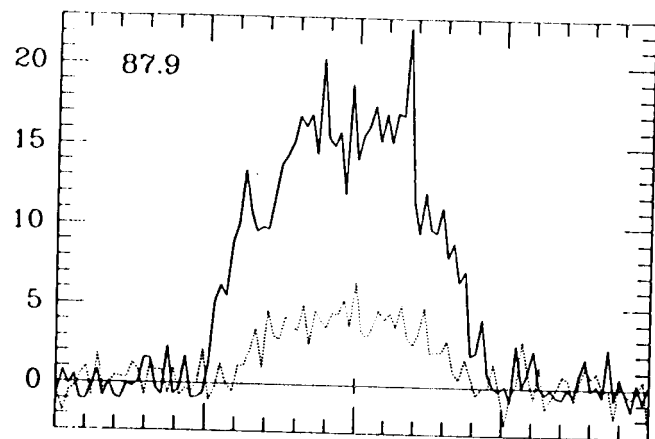


Geographos SC/OC



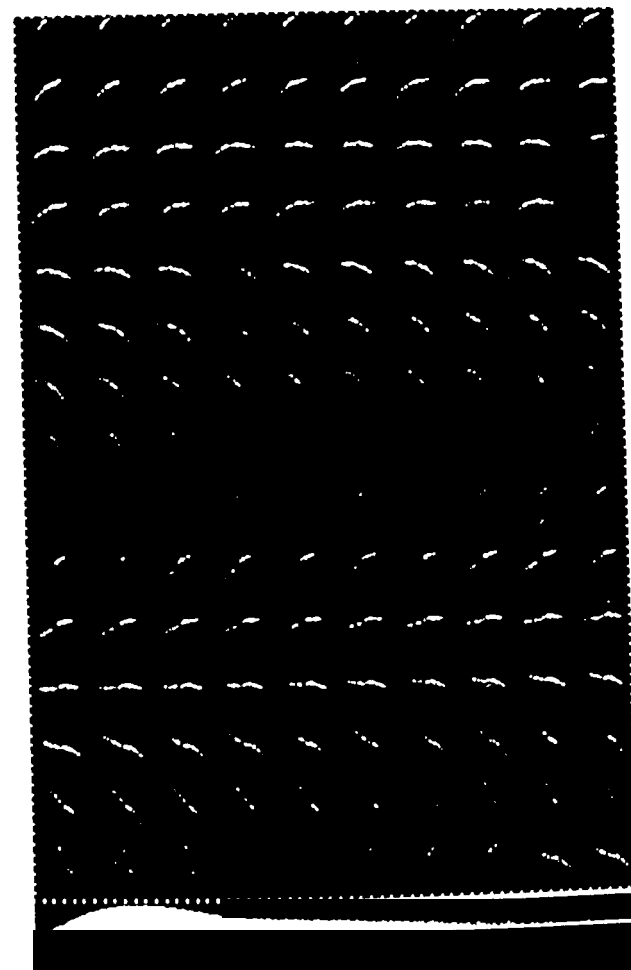


Ostro *et al.* Fig. 6

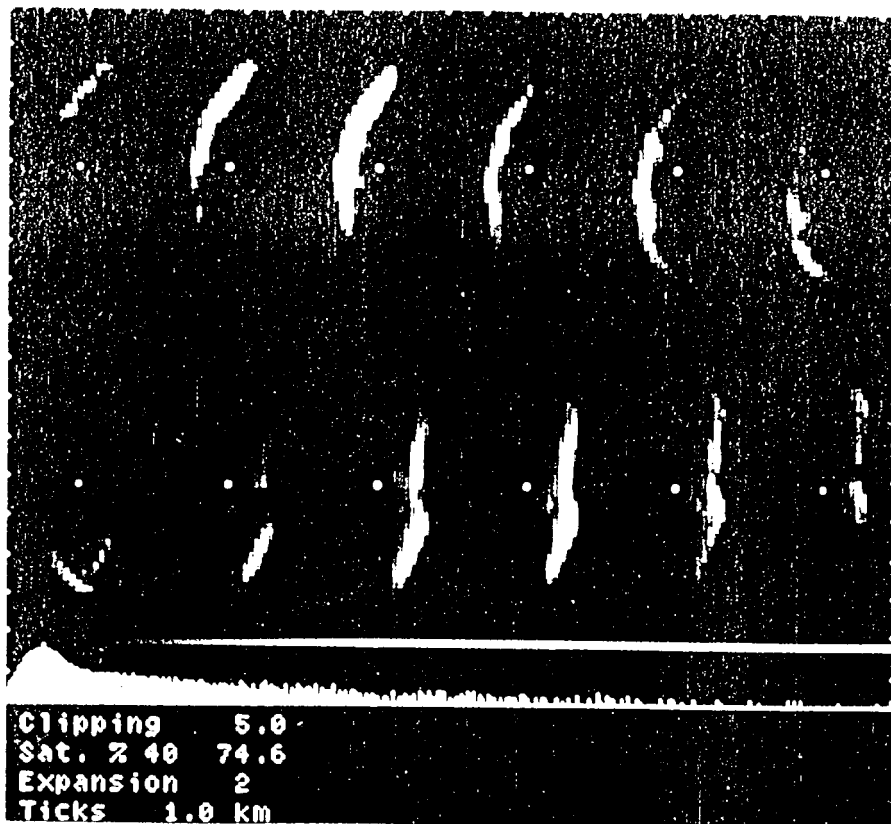


Ge 007	{	2	6	9	13	18	20	22	25	27	}	Ge 007
		29	32	34	36	39	41	43	50	52		Ge 008
Ge 008	{	57	59	62	64	66	69	71	73	76	}	Ge 103
		47	49	52	54	56	59	61	63	65		Ge 104
Ge 104	{	87	90	92	94	97	99	101	104	106	}	Ge 104
		110	118	115	117	120	122	124	127	129		
		134	136	138	140	143	145	147	150	153		
		161	164	166	168	170	173	175	177	180		
Ge 105	{	184	187	190	191	194	196	205	208	210	}	Ge 105
		214	217	219	221	224	226	228	231	233		
		237	240	242	244	247	249	251	253	256		
		260	263	265	267	270	272	274	277	279		
Ge 106	{	283	292	294	296	299	303	305	308	310	}	Ge 106
		315	317	319	322	324	326	328	331	333		
Ge 106	{	338	340	347	349	357	10	5	15	290	}	Ge 203
										292		

a



b



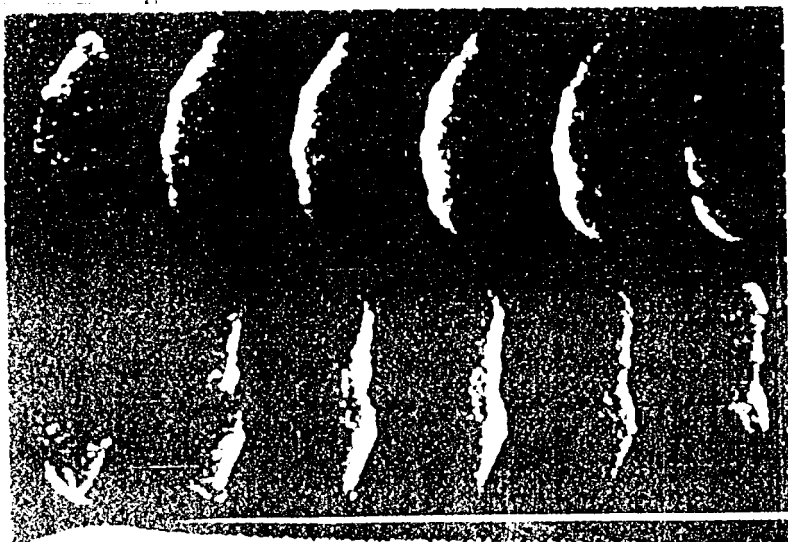
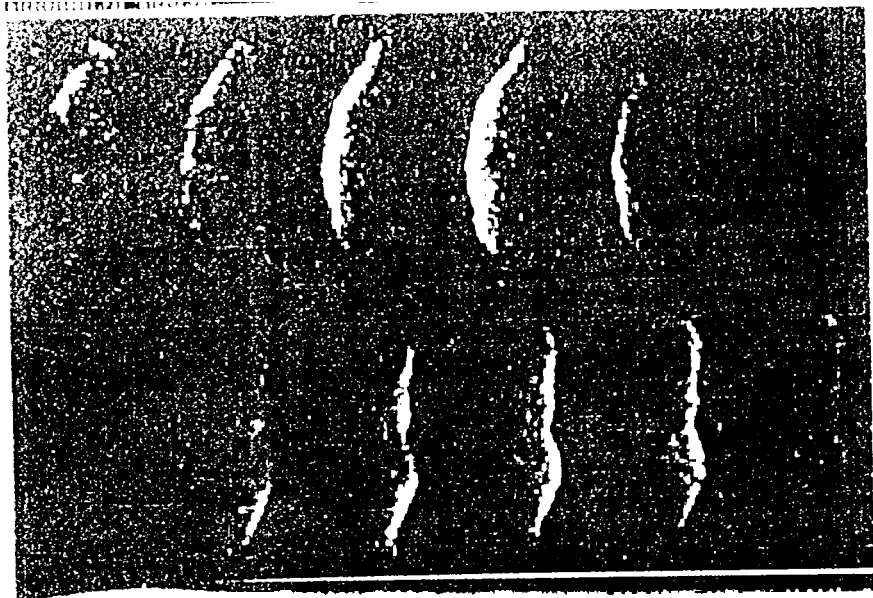
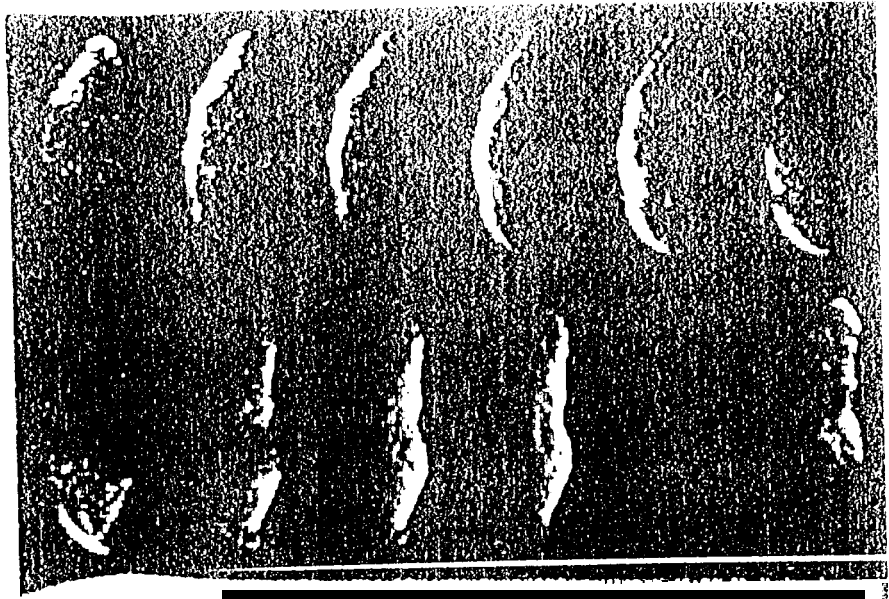
Ostro *et al.* Fig. 9

a



Ostro et al., Fig. 10

a
b
c



Slipping: 0.0
Acc: 0.0
Expansion: 2
Ticks: 1.0 km
Date: 11/11/87

Ostroet al. Fig. 11